The Astrophysical Journal, 756:151 (15pp), 2012 September 10 doi:10.1088/0004-637X/756/2/151

TRIGGERED STAR FORMATION AROUND MID-INFRARED BUBBLES IN THE G8.14+0.23 H II REGION

L. K. Dewangan[1], D. K. Ojha[1], B. G. Anandarao[2], S. K. Ghosh[3], and S. Chakraborti[1]
[1] Department of Astronomy and Astrophysics, Tata Institute of Fundamental Research, Homi Bhabha Road, Mumbai 400 005, India; lokeshd@tifr.res.in
[2] Physical Research Laboratory, Navrangpura, Ahmedabad 380 009, India
[3] National Centre for Radio Astrophysics, Ganeshkhind, Pune 411 007, India
Received 2012 May 17; accepted 2012 July 29; published 2012 August 23

ABSTRACT

Mid-infrared shells or bubbles around expanding H II regions have received much attention due to their ability to initiate a new generation of star formation. We present multi-wavelength observations around two bubbles associated with a southern massive star-forming region G8.14+0.23, to investigate the triggered star formation signature on the edges of the bubbles by the expansion of the H II region. We have found observational signatures of the collected molecular and cold dust material along the bubbles and the ^{12}CO(J = 3–2) velocity map reveals that the molecular gas in the bubbles is physically associated around the G8.14+0.23 region. We have detected 244 young stellar objects (YSOs) in the region and about 37% of these YSOs occur in clusters. Interestingly, these YSO clusters are associated with the collected material on the edges of the bubbles. We have found good agreement between the dynamical age of the H II region and the kinematical timescale of bubbles (from the ^{12}CO(J = 3–2) line data) with the fragmentation time of the accumulated molecular materials to explain possible "collect and collapse" process around the G8.14+0.23 region. However, one cannot entirely rule out the possibility of triggered star formation by compression of the pre-existing dense clumps by the shock wave. We have also found two massive embedded YSOs (about 10 and 22 $M_{\odot}$) which are associated with the dense fragmented clump at the interface of the bubbles. We conclude that the expansion of the H II region is also leading to the formation of these two young massive embedded YSOs in the G8.14+0.23 region.

Key words: dust, extinction – H II regions – ISM: bubbles – ISM: individual objects (IRAS 17599-2148) – stars: formation – stars: pre-main sequence

Online-only material: color figures

1. INTRODUCTION

Massive stars have a major impact on their surrounding environment due to their energetic wind, UV ionizing radiation, and an expanding H II region (Zinnecker & Yorke 2007). In recent years, Mid-infrared (MIR) shells or bubbles around the expanding H II regions have received much attention because of their ability to initiate a new generation of star formation (Watson et al. 2008, 2009, 2010). Churchwell et al. (2006, 2007) identified about 600 such shells or bubbles based on a circular morphology in *Spitzer–GLIMPSE* 8 μm emission. It is now believed that such regions are very promising to observationally study the conditions of sequential/triggered star formation (Thompson et al. 2012, and references therein).

In this paper, we present a study of two MIR bubbles, CN107 and CN109, from the catalog of Churchwell et al. (2007) around the G8.14+0.23 region. The G8.14+0.23 is an irregular Galactic ultracompact (UC) H II region close to the IRAS 17599-2148 source, situated at a distance of 4.2 kpc (Kim & Koo 2001). The G8.14+0.23 region has been extensively studied in the radio, submillimeter, and molecular line observations (Codella et al. 1994; Walsh et al. 1997, 1998; Kim & Koo 2001, 2003; Ojeda-May et al. 2002; Thompson et al. 2006). The region is ionized by an O6(B0) spectral class source and is also known as a bipolar blister type H II region due to a champagne flow (Kim & Koo 2001, 2003). The 6.7 GHz Class II methanol maser (Walsh et al. 1997, 1998) and water maser (Codella et al. 1994) were also detected close to the *IRAS* position. The site of massive star formation is often associated with methanol and water maser emission. Kim & Koo (2001) found the velocity of ionized gas to be about 20.3 km s^{-1} close to the *IRAS* position, using H76α recombination line profile. The velocity of molecular flow was obtained to be about 19.6 km s^{-1} using CS J = 2–1 lines by Kim & Koo (2003). These velocities are close to the values obtained by NH_3(2,2) and (4,4) emissions to be about 19.3 km s^{-1} (Churchwell et al. 1990) and 20.3 km s^{-1} (Cesaroni et al. 1992), respectively. Kim & Koo (2003) found irregular morphology and clumpy structure of molecular cloud around G8.14+0.23, using ^{13}CO (J = 1–0) and CS (J = 2–1) line intensity maps. Kim & Koo (2003) and Thompson et al. (2006) also found a molecular and dust emission ridge around the region. Okada et al. (2008) analyzed the MIR spectroscopic observations using *Spitzer*-Infrared Spectrograph (IRS) for 14 Galactic star-forming regions, including G8.14+0.23, in the wavelength range of 20–36.5 μm. They argued the presence of the shocked and ionized gas associated with the G8.14+0.23 region, based on the detection of [Si II], [Fe II], and [S III] emission lines and derived the abundance ratio of two ions against the solar abundance ("as") as 0.060, 0.158, and 0.020 for $(Fe^{+}/Si^{+})_{as}$, $(Si^{+}/S^{2+})_{as}$, and $(Fe^{2+}/S^{2+})_{as}$, respectively.

In recent years, multi-wavelength observations are utilized to trace out different components associated with the star-forming regions, viz., ionized, shocked, cold dust, and molecular gas, as well as embedded young stellar populations. In this paper, we present multi-wavelength observations to investigate the triggered star formation around the MIR bubbles associated with a southern massive star-forming (MSF) region G8.14+0.23. This region is not well explored in infrared wavelengths, especially the identification of embedded populations around the region. Our study also includes the search for the infrared counterpart(s) of embedded massive young stellar objects (YSOs) in their earlier phases and to understand their formation processes.

In Section 2, we introduce the archival data and data reduction procedures used for the present study. In Section 3, we examine the morphology of the G8.14+0.23 region in different wavelengths and the interaction of massive stars with its environment using various *Spitzer* MIR ratio maps. We also describe the selection of young population, their distribution around the G8.14+0.23 region and discuss the triggered star formation scenario on the edge of the bubbles in this section. In Section 4, we summarize our conclusions.

2. AVAILABLE DATA AROUND G8.14+0.23 AND DATA REDUCTION

Archival deep near-infrared (NIR) JHK_s images and catalog of G8.14+0.23 region were obtained from the UKIDSS sixth archival data release (UKIDSSDR6plus) of the Galactic Plane Survey (GPS; Lawrence et al. 2007). UKIDSS observations were made using the UKIRT Wide-Field Camera (Casali et al. 2007) and fluxes were calibrated using Two Micron All Sky Survey (2MASS; Skrutskie et al. 2006). The details of basic data reduction and calibration procedures are described in Dye et al. (2006) and Hodgkin et al. (2009), respectively. Magnitudes of bright stars ($J \leqslant 11.5$ mag, $H \leqslant 11.5$ mag, and $K_s \leqslant 10.5$ mag) were obtained from the 2MASS, due to saturation of UKIDSS bright sources. Only those sources are selected for the study which have photometric magnitude error of 0.1 and less in each band.

We obtained narrowband molecular hydrogen (H_2; 2.12 μm; 1–0 S(1)) imaging data from UWISH2 survey (Froebrich et al. 2011). We followed a similar procedure as described by Varricatt (2011) to obtain the final continuum-subtracted H_2 image using GPS K_s image.

The *Spitzer Space Telescope* Infrared Array Camera (IRAC Ch1 (3.6 μm), Ch2 (4.5 μm), Ch3 (5.8 μm), and Ch4 (8.0 μm); Fazio et al. 2004) and Multiband Imaging Photometer (MIPS (24 μm); Rieke et al. 2004) archival images were obtained around the G8.14+0.23 region from the "*Galactic Legacy Infrared Mid-Plane Survey Extraordinaire*" (*GLIMPSE*) and "A 24 and 70 Micron Survey of the Inner Galactic Disk with MIPS" (MIPSGAL) surveys (Benjamin et al. 2003; Churchwell et al. 2009; Carey et al. 2005). MIPSGAL 24 μm image is saturated close to the IRAS 17599-2148 position. We performed aperture photometry on all the *GLIMPSE* images (plate scale of 0.6 arcsec pixel^{-1}) using a 2.4 arcsec aperture and a sky annulus from 2.4 to 7.3 arcsec using IRAF.[4] The photometry is calibrated using zero mag including aperture corrections, 18.5931 (Ch1), 18.0895 (Ch2), 17.4899 (Ch3), and 16.6997 (Ch4), obtained from IRAC Instrument Handbook (Version 1.0, 2010 February).

We obtained 20 cm radio continuum map (resolution ~6 arcsec) from Very Large Array (VLA) Multi-Array Galactic Plane Imaging Survey (MAGPIS; Helfand et al. 2006) to trace the ionized region around G8.14+0.23. The molecular ^{12}CO(J = 3–2) (rest frequency 345.7959899 GHz) spectral line public processed archival data was also utilized in the present work. The CO observations were taken on 2009 June 11 at the 15 m James Clerk Maxwell Telescope (JCMT) using the HARP array. The JCMT archival reduced fits cube was used to extract the velocity information around the region using the Astronomical Image Processing System[5] (AIPS) package. The fits cube was loaded into AIPS and rotated to make the frequency axis the first one. An alternate velocity axis was defined from the frequency using the rest-frame frequency of the CO J = 3–2 transition. The data were Hanning smoothed over 476 m s^{-1} to decrease the noise per channel. It was then integrated over the velocity range 10–30 km s^{-1} to obtain the zeroth moment (column density), first moment (mean velocity), and second moment (velocity dispersion). Archival BOLOCAM 1.1 mm (Aguirre et al. 2011) and SCUBA 850 μm (Di Francesco et al. 2008) images were also used in the present work. The effective FWHM Gaussian beam sizes of final 1.1 mm and 850 μm images were 33 arcsec and 22.9 arcsec, respectively.

[4] IRAF is distributed by the National Optical Astronomy Observatory, USA.
[5] http://www.aips.nrao.edu/

3. RESULTS AND DISCUSSION

3.1. Morphology of the G8.14+0.23 Region in Different Wavelengths

Figure 1(a) represents the RGB color composite image using *GLIMPSE* (8.0 μm (red) and 4.5 μm (green)) and UKIDSS K_s (blue) of a region (~6.6 × 5.9 arcmin^2) around G8.14+0.23. The 8 μm band contains the two strongest polycyclic aromatic hydrocarbon (PAH) features at 7.7 μm and 8.6 μm, which are excited in the photodissociation region (or photon-dominated region or PDR). The PDRs are the interface between neutral and molecular hydrogen and traced by PAH emissions. Figure 1(b) shows the three-color composite image using UKIDSS J (blue), H (green), and K_s (red) band in log scale. The positions of IRAS 17599-2148 (★), UC H II region (◇), methanol maser (+), and water maser (×) are marked in the figure. The coordinates of UC H II region, methanol maser, and water maser were taken from Kim & Koo (2001), Walsh et al. (1998) and Codella et al. (1994), respectively. Figure 1(a) displays the two extended MIR bubbles CN107 and CN109 prominently around the G8.14+0.23 region. It is to be noted that these bubble structures are not visible in any of the UKIDSS NIR images (see Figure 1(b)), but dark regions are seen corresponding to the bubble structures in Figure 1(b). The two infrared sources (designated as IRS 1 and IRS 2) are seen close to the *IRAS* position and are also marked in Figure 1(a) (see Section 3.3.1 for more details). Figure 2 shows the color composite image made using MIPSGAL 24 μm (red), *GLIMPSE* 8 μm (green), and 3.6 μm (blue) images, overlaid by BOLOCAM 1.1 mm and SCUBA 850 μm emission by dotted white and solid yellow contours, respectively. The MIPS 24 μm image is saturated near to the *IRAS* position. MAGPIS 20 cm radio continuum emission is also overlaid in Figure 2 by black contours. The cold dust emission at 850 μm is very dense and prominent at the interface of the two bubbles. It is to be noted that the peaks of cold dust and ionized gas are concentrated near the *IRAS* position and interface of the bubbles. The 24 μm and 20 cm images trace the warm dust and ionized gas in the region, respectively. It is obvious from Figure 2 that the PDR region (traced by 8 μm) encloses 24 μm and 20 cm radio emissions inside the bubbles and indicates the presence of dust in and around the H II region (see, for example, Watson et al. 2008 for N10, N21, and N49 bubbles).

3.2. IRAC Ratio Maps and the Collected Material

In recent years, *Spitzer*-IRAC bands and ratio maps are utilized to study the interaction of massive stars with its immediate environment (Povich et al. 2007). The IRAC bands contain a number of prominent atomic and molecular lines/features such as H_2 lines in all channels (see Table 1 from Smith & Rosen 2005), Brα 4.05 μm (Ch2), Fe II 5.34 μm (Ch3), Ar II 6.99 μm, and Ar III 8.99 μm (Ch4) (see Reach et al. 2006). It is

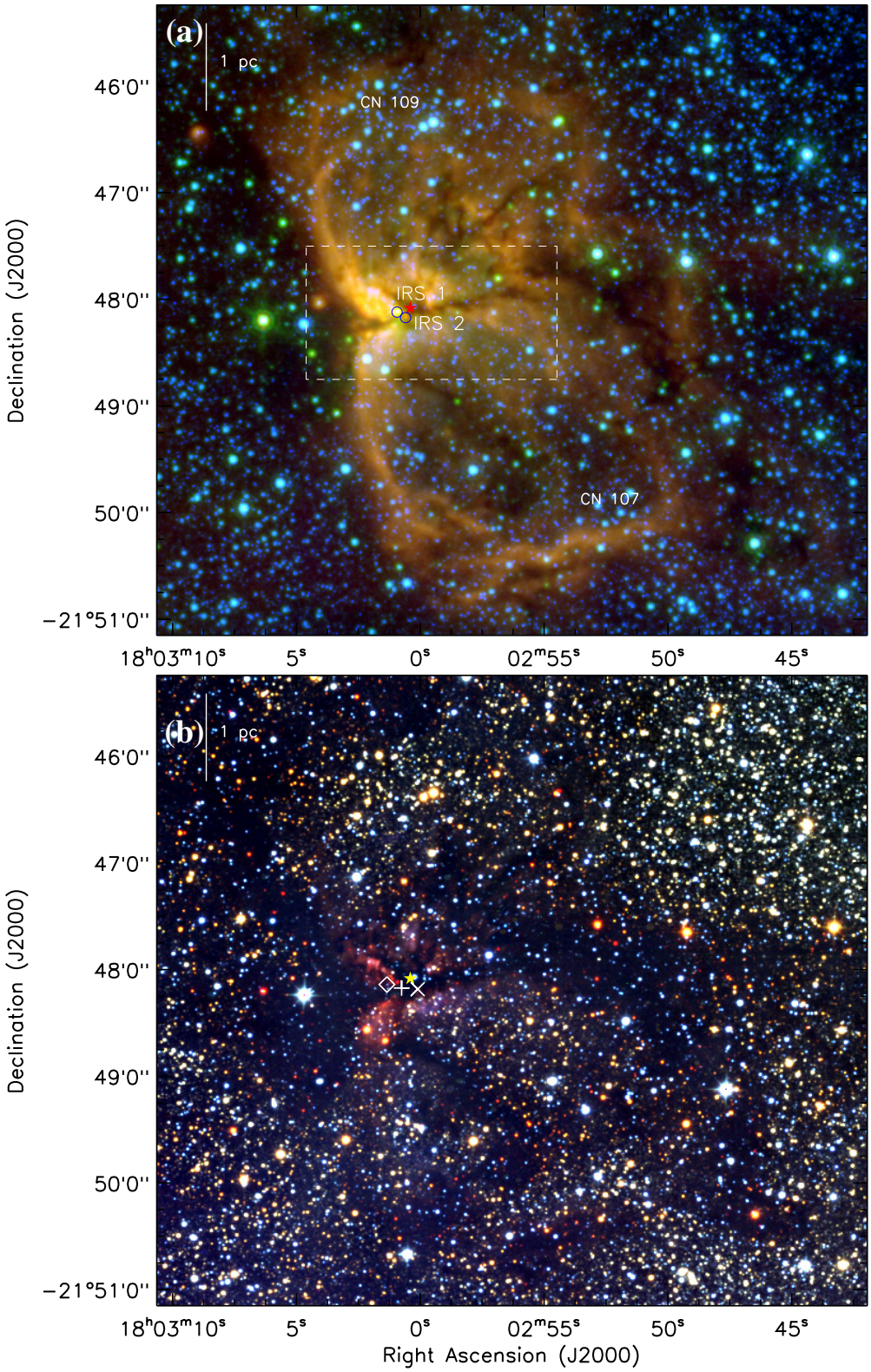

Figure 1. (a) Three-color composite image (size ∼6.6 × 5.9 arcmin^2; central coordinates: α_{2000} = 18^{h}02^{m}56.3, δ_{2000} = −21°48′12.″6) of the G8.14+0.23 region, using *Spitzer–GLIMPSE* images at 8.0 μm (red), 4.5 μm (green), and UKIDSS K_s (blue) in log scale. The positions of the two sources (IRS 1 and IRS 2) are marked by blue circles and labeled on the image. The scale bar on the top left shows a size of 1 pc at the distance of 4.2 kpc. The white dashed box is shown as zoomed-in view in Figure 8. Two bubbles from Churchwell et al. (2007) are also labeled on the image as CN 107 and CN 109. (b) Color composite image using UKIDSS J (blue), H (green), and K_s (red) in log scale. The positions of IRAS 17599-2148 (★), UC H II region (◇), methanol maser (+), and water maser (×) are marked in the figure.
(A color version of this figure is available in the online journal.)

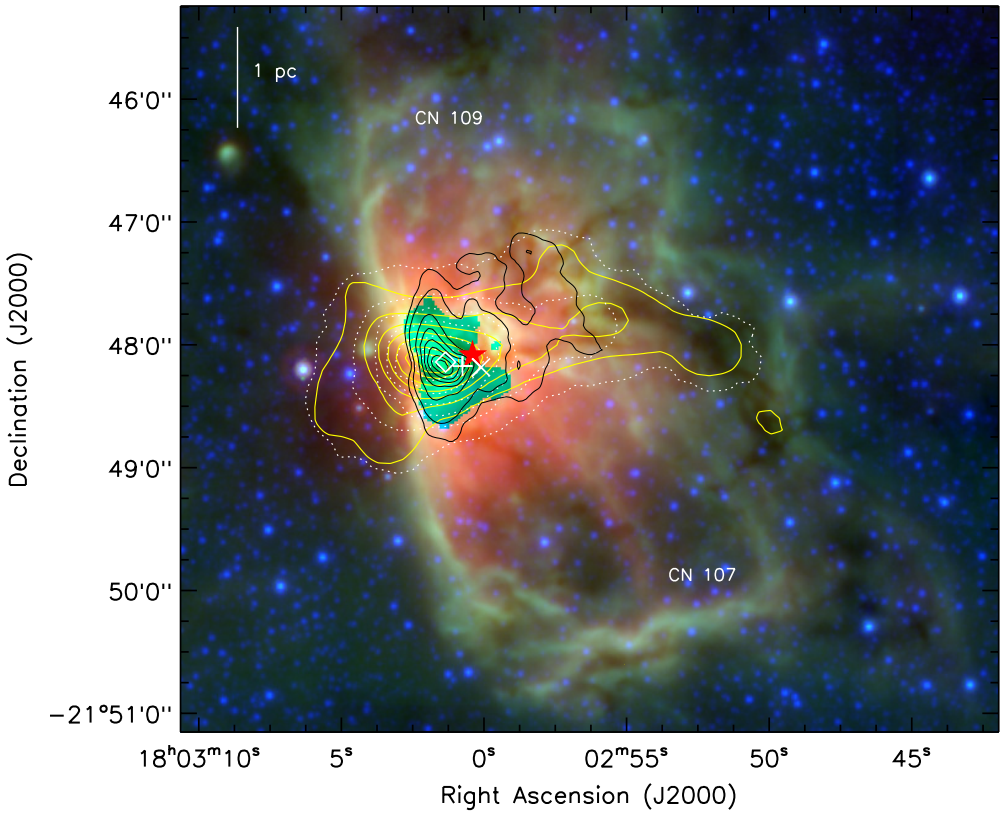

Figure 2. Representation of 20 cm contours in black color around the G8.14+0.23 region obtained from the MAGPIS survey, overlaid on a color composite image made using the 24 μm (red), 8 μm (green), and 3.6 μm (blue) images. The 20 cm contour levels are 10%, 25%, 40%, 55%, 70%, 85%, and 95% of the peak value, i.e., 0.23 Jy beam^{-1}. BOLOCAM 1.1 mm and SCUBA 850 μm emissions are also shown by dotted white and solid yellow contours with 10%, 25%, 40%, 55%, 70%, 85%, and 95% of the peak value, i.e., 3.55 and 8.23 Jy beam^{-1}, respectively. Two bubbles from the Churchwell et al. (2007) are also labeled on the image as CN 107 and CN 109. The marked symbols are similar to as shown in Figure 1 (see the text for more details). The MIPS 24 μm image is saturated near to the *IRAS* position. (A color version of this figure is available in the online journal.)

to be noted that the *Spitzer*-IRAC bands, Ch1, Ch3, and Ch4, contain the PAH features at 3.3, 6.2, 7.7, and 8.6 μm, whereas Ch2 (4.5 μm) does not include any PAH features. Therefore, IRAC ratio (Ch4/Ch2, Ch3/Ch2, and Ch1/Ch2) maps are being used to trace out the PAH features in MSF regions (e.g., Povich et al. 2007; Watson et al. 2008; Kumar & Anandarao 2010) due to UV radiation from massive star(s). In order to make the ratio maps, we generate residual frames for each band removing point sources by choosing an extended aperture (12.2 arcsec) and a larger sky annulus (14.6–24.4 arcsec; Reach et al. 2005) in IRAF/DAOPHOT software (Stetson 1987). These residual frames are then subjected to median filtering with a width of 10 pixels and smoothing by 3 × 3 pixels using the boxcar algorithm (e.g., Povich et al. 2007). Figures 3(a) and (b) represent the IRAC ratio maps, Ch3/Ch2 and Ch4/Ch2 around the G8.14+0.23 region, respectively. The ratio contours are also overlaid on the ratio maps for better clarity and insight (see Figure 3). Both the ratio maps clearly trace the prominent PAH emissions and subsequently extent of PDRs in the region.

Figure 4 shows the IRAC Ch2/Ch1 ratio map overlaid with the Ch3/Ch2 ratio and MAGPIS 20 cm radio contours. The bright region traced by the Ch2/Ch1 ratio map is coincident with the 20 cm radio continuum emission, possibly due to the presence of the Brα (4.05 μm) feature in the Ch2 band around the H II region. One can also note very faint diffuse emission along the edges of the bubbles away from the peak of the 20 cm radio emission, possibly due to the molecular hydrogen feature in the Ch2 band. Ojeda-May et al. (2002) detected two sources in the 6 cm radio observations around the G8.14+0.23 region. The positions of these sources are also shown in Figure 4. Figures 5(a)–(c) show the gray-scale images in SCUBA 850 μm, BOLOCAM 1.1 mm, and JCMT CO 3–2 (345.79599 GHz) around the G8.14+0.23 region, respectively. Figure 5 exhibits the evidence of collected material along the bubbles traced by dust continuum (SCUBA 850 μm and BOLOCAM 1.1 mm) and molecular gas (JCMT CO 3–2 at 345.79599 GHz) emission, which is also indicated by red arrows. These arrows are marked to show the associated faint features above the 4σ noise level for each image. We further utilized JCMT public processed CO 3–2 cube data to observationally check the association of the molecular material with the expanding H II region seen as MIR bubbles. We calculated the mean H_2 number density near the H II region using the ^{12}CO zeroth moment map. We derived the column density using the formula N_{H_2} (cm^{-2}) = $X \times W_{CO}$, where $X = 6 \times 10^{20}$ cm^{-2} K^{-1} km^{-1} s (see Ji et al. 2012) and $W_{CO} = 48.08$ K km s^{-1} from our map. The mean H_2 number density is obtained to be 3575.7 cm^{-3} using the relation N_{H_2} (cm^{-2})/L (cm), where L is the molecular core size of about 8.07×10^{18} cm (~2.6 pc) near the H II region. Figure 6 exhibits molecular emission around the region between 17 and 25 km s^{-1} velocity interval in steps of 1 km s^{-1}. The bubbles (CN 107 and CN 109) are clearly traced by molecular emission in the velocity range of 19–21 km s^{-1} (see Figure 6). We also estimated velocity dispersion of about 4 km s^{-1} (using second moment CO map) around the region, assuming a smooth rotation curve for the Galaxy with typical gas dispersion velocity of about

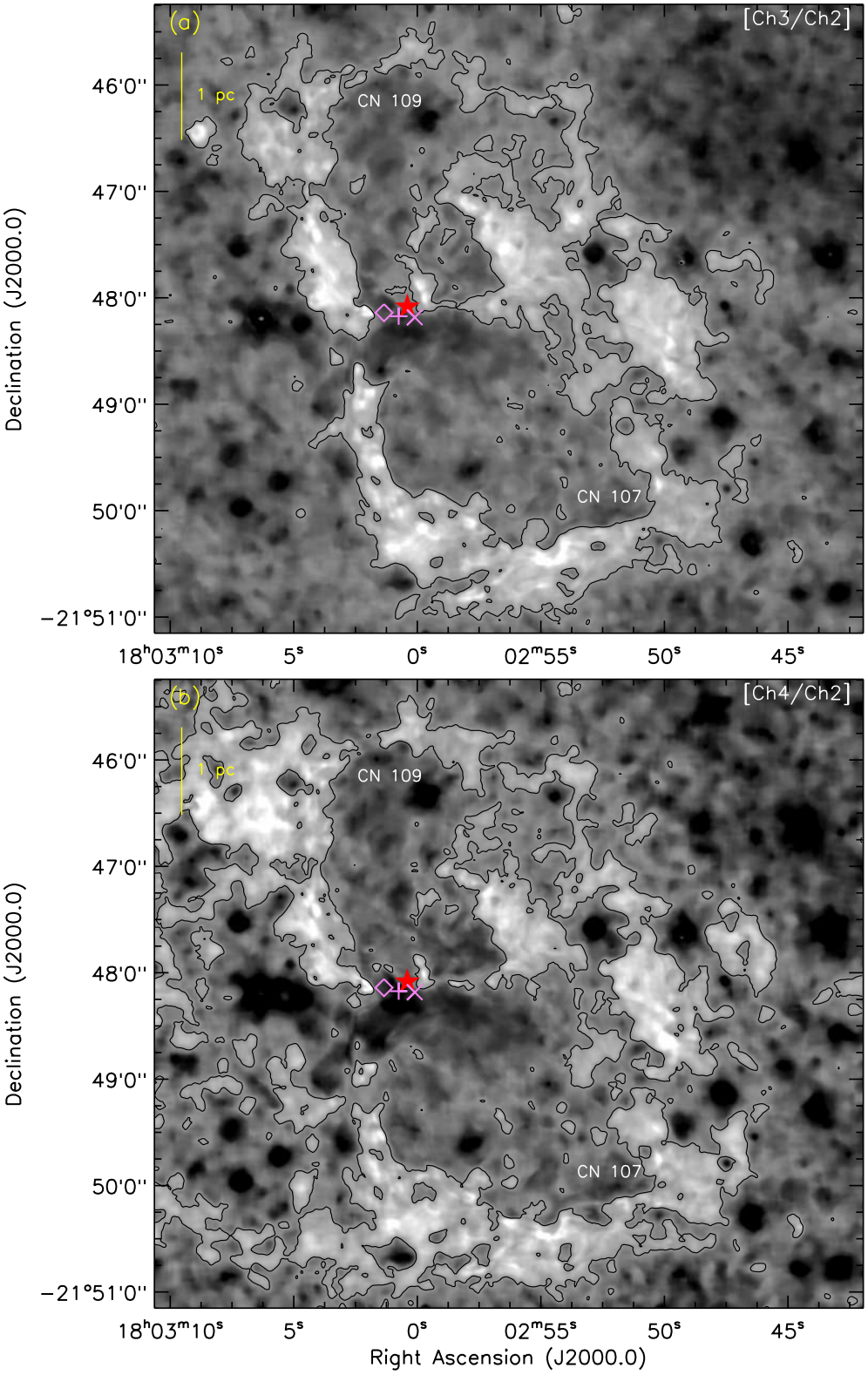

Figure 3. (a) *GLIMPSE* Ch3/Ch2 ratio map of the G8.14+0.23 region (similar area as shown in Figure 1). The ratio Ch3/Ch2 value is found to be "7–8" and "8.5–9" in the bubble interior and for the brightest part of the PDR, respectively. The Ch3/Ch2 ratio contours are also overlaid on the image with a level of 7.7, a representative value between "7 and 8." (b) The Ch4/Ch2 ratio map of the region is shown here. The ratio Ch4/Ch2 value for the brightest part of the PDR and the interior is "30–34" and "23–25," respectively. The Ch4/Ch2 ratio contours are also overlaid on the image with a level of 24.8, a representative value between "23 and 25." The marked symbols are similar to as shown in Figure 1.

(A color version of this figure is available in the online journal.)

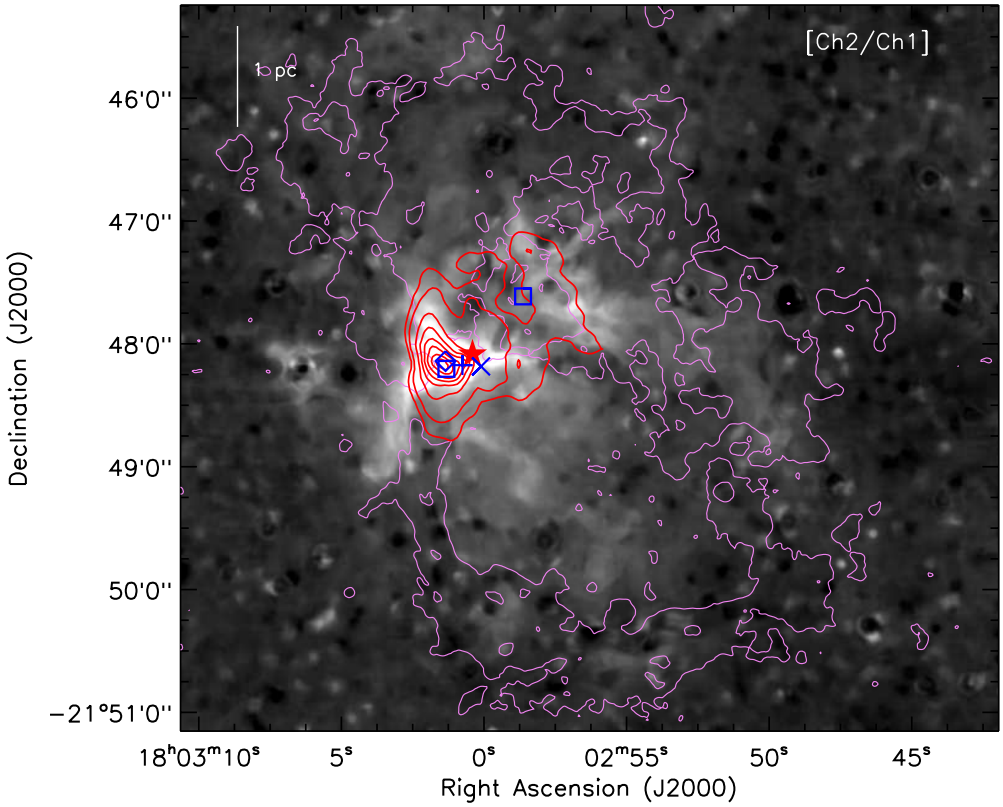

Figure 4. Ch2/Ch1 ratio image of the G8.14+0.23 region. The Ch3/Ch2 ratio contours in violet are also overlaid on the image with a level of 7.7. Contours in red represent the 20 cm radio continuum emission with similar levels as shown in Figure 2 around the region. Square symbols represent the 6 cm radio detections by Ojeda-May et al. (2002) and other marked symbols are similar to as shown in Figure 1.

(A color version of this figure is available in the online journal.)

10 km s^{-1} (Stark & Brand 1989; Silk 1997). The consideration of velocity ranges of molecular gas in which bubbles are traced (see Figure 6) and the velocity dispersion value imply that the molecular gas in these bubbles are physically associated. These velocity ranges of molecular gas are also compatible with the ionized gas velocity (∼20.3 km s^{-1}) obtained by the H76α recombination line profile study around the H II region (Kim & Koo 2001), which shows the physical association of the molecular material and the H II region. The evidence of collected material along the bubbles is further confirmed by the detection of the H_2 emission (see Figure 7). Figure 7 represents the continuum-subtracted H_2 image at 2.12 μm and reveals that the H_2 emission surrounds the H II region along bubbles, forming a PDR region, which may be collected due to the shock. In brief, the PAH emission, cold dust emission, molecular CO gas, and shocked H_2 emissions are coincident along the bubbles.

Figure 8 exhibits the zoomed-in color composite image using IRAC/*GLIMPSE* images (red: 8.0 μm, green: 5.8 μm, and blue: 4.5 μm) around the G8.14+0.23 region. The slit positions of *Spitzer*-IRS spectrograph at eight observed locations around the G8.14+0.23 region are also marked in Figure 8 with star symbols (see Okada et al. 2008). Okada et al. (2008) also listed the line intensities of detected emission lines ([Ar III], 22 μm; [Fe III], 23 μm; [Fe II], 26 μm; H_2 0–0 S(0), 28 μm; [S III], 33 μm; [Si II], 35 μm; and [Ne III], 36 μm) at the eight observed positions (similar labels marked as 0–7 in Figure 8) around the G8.14+0.23 region. The presence of both PAH and fine structure line emissions around the region clearly suggests the presence of an ionizing source with UV radiation close to radio and dust continuum peaks.

3.3. Photometric Analysis of Point-like Sources Around the G8.14+0.23 Region

In order to trace ongoing star formation activity in the G8.14+0.23 region, we have identified YSOs using NIR and *GLIMPSE* data.

3.3.1. Identification of YSOs

We have used Gutermuth et al. (2009) criteria based on four IRAC bands to identify YSOs and various possible contaminants (e.g., broad-line active galactic nuclei, PAH-emitting galaxies, shocked emission blobs/knots, and PAH-emission-contaminated apertures). These YSOs are further classified into different evolutionary stages (i.e., Class I, Class II, Class III, and photospheres) using slopes of the IRAC spectral energy distribution (SED). Figure 9(a) shows the IRAC color–color ([3.6]−[4.5] versus [5.8]−[8.0]) diagram for all the identified sources. We find 14 YSOs (6 Class 0/I and 8 Class II), 2 Class III, 123 photospheres, and 8 contaminants in the G8.14+0.23 region. Two sources close to the peak of the dense molecular gas and the dust clump at the interface of the bubbles, IRS 1 and IRS 2, are also labeled in Figure 9(a). The position of IRS 2 is shown by a star symbol using 3.6 μm mag as an upper limit (see Table 1). It is to be noted that IRS 2 is close (about 2 arcsec) to the detected methanol maser. The details of the YSO classification can be found in Dewangan & Anandarao (2011). We have also applied criteria to identify YSOs as suggested by Hartmann et al. (2005) and Getman et al. (2007) for those sources that are detected in three IRAC/*GLIMPSE* bands, but not in the 8.0 μm band. We identify 12 more YSOs (2 Class 0/I; 10 Class II) through

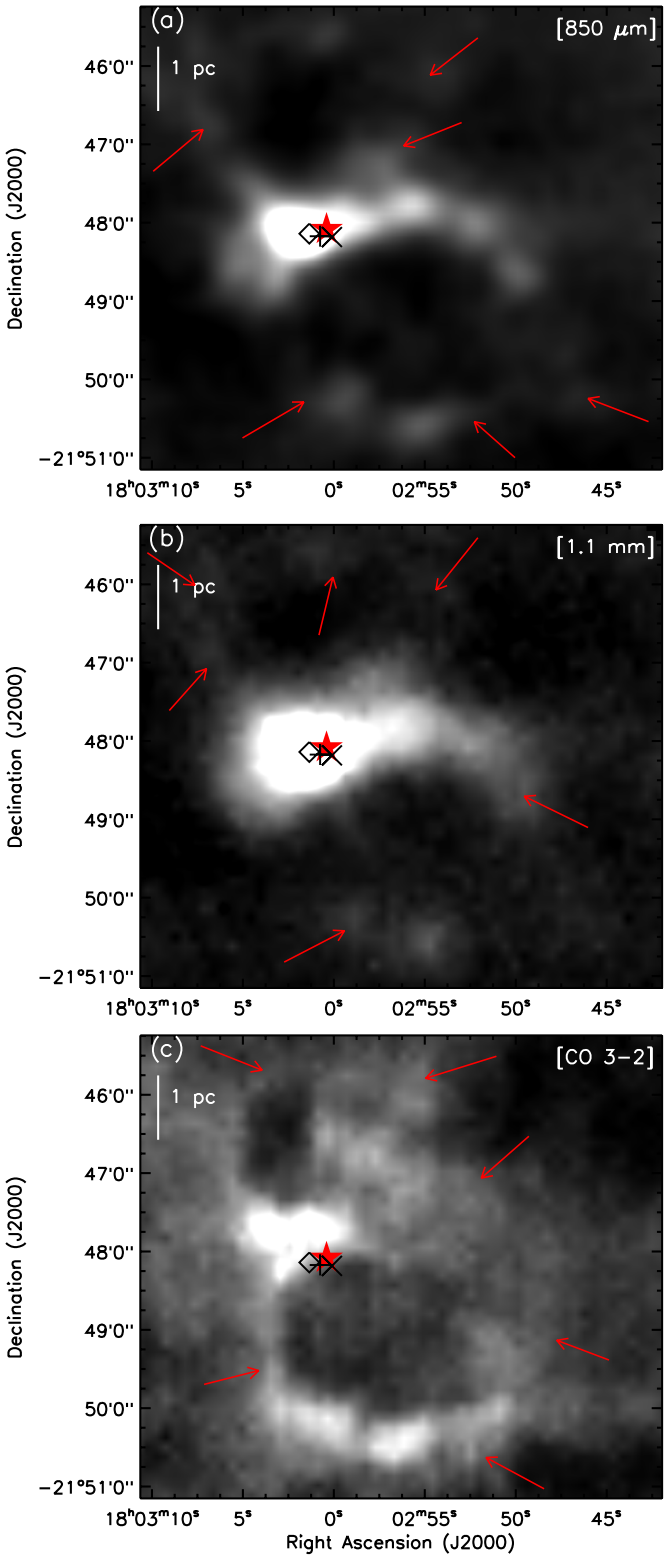

Figure 5. Gray-scale image in SCUBA 850 μm (a), BOLOCAM 1.1 mm (b), and JCMT CO 3–2 (c) around the G8.14+0.23 region, respectively. Red arrows show the detected faint features around the G8.14+0.23 region and other marked symbols are similar to as shown in Figure 1.

(A color version of this figure is available in the online journal.)

color–color diagram (CCD) using three *GLIMPSE* bands in the region (see Figure 9(b)).

UKIDSS NIR JHK_s photometry is used to identify more YSOs in the region. NIR CCD ($H - K_s/J - H$) is shown in Figure 9(c) for all the sources detected in J, H, and K_s bands. We have divided the CCD into three regions, namely, "F," "T," and "P" (e.g., Sugitani et al. 2002; Ojha et al. 2004a, 2004b). The "F" sources are located between the reddening bands of the main-sequence and giant stars. The sources located within the "T" region along the T Tauri locus are T Tauri-like sources (Class II objects) with large NIR excess. "P" sources are those located in the region redward of region "T," and are most likely Class I objects (protostellar objects). We have identified 159 Class II and 30 Class I sources located in the "T" and "P" regions in Figure 9(c), respectively. The identified Class I and Class II sources are shown by red circles and blue triangles in Figure 9(c). We have estimated the visual extinction (A_V) using the CCD and following the Indebetouw et al. (2005) extinction law, for those sources that fall within the "F" region (see Ojha et al. 2010). The average value comes out to be $A_V \sim$ 8.2 mag, which is in good agreement with that estimated ($A_V \sim$ 8.8 mag) by Rowles & Froebrich (2009) using 2MASS data for the G8.14+0.23 region.

GLIMPSE 3.6 and 4.5 μm bands are more sensitive for point sources than *GLIMPSE* 5.8 and 8.0 μm images. Therefore, a larger number of YSOs can be identified using a combination of NIR (JHK_s) with *GLIMPSE* 3.6 and 4.5 μm (i.e., NIR-IRAC) photometry, where sources are not detected in IRAC 5.8 and/or 8.0 μm band (Gutermuth et al. 2009). We followed the criteria given by Gutermuth et al. (2009) to identify YSOs using H, K_s, 3.6 and 4.5 μm data. We have found 29 more YSOs (26 Class II and 3 Class I) using NIR-IRAC data (see Figure 9(d)).

Finally, we have obtained a total of 244 YSOs (203 Class II and 41 Class I) using NIR and *GLIMPSE* data in the region.

3.3.2. YSOs Surface Density Map

To study the spatial distribution of YSOs, we generated the surface density map of all YSOs using a 5 arcsec grid size, following the same procedure as given in Gutermuth et al. (2009). The surface density map of YSOs is constructed using six nearest-neighbor (NN) YSOs for each grid point. Figure 10(a) shows the spatial distribution of all identified YSOs (Class I and Class II) in the region. The contours of YSO surface density and Ch3/Ch2 ratio map are also overlaid on the diagram. The levels of YSO surface density contours are 6 (2.5σ), 8 (3.3σ), 11 (4.6σ), and 16 (6.7σ) YSOs pc^{-2}, increasing from the outer to the inner region. We have also calculated the empirical cumulative distribution (ECD) as a function of NN distance to identify the clustered YSOs in the region. Using the ECD, we estimate the distance of inflection $d_c = 0.617$ pc (0.0084 deg at 4.2 kpc) for the region for a surface density of 6 YSOs pc^{-2} (see Dewangan & Anandarao 2011 for details of d_c and ECD). We find that 37% (91 out of 244 YSOs) YSOs are present in clusters. Figure 10(a) reveals that the distribution of YSOs is mostly concentrated in the north and east regions, having peak density of about 20 YSOs pc^{-2}, while YSO density of about 8 (3σ) YSOs pc^{-2} is also seen around the west and southeast regions (see Figure 10(a)). These values of YSO surface density are much lower than usual values (about 30–60 YSOs pc^{-2}) found in recent works (see Gutermuth et al. 2009, 2011) in MSF regions. Also the percentage of YSOs in clusters is low (only 37%) as compared to recent reports (about 60%–80%) in MSF regions (see Gutermuth et al. 2009, 2011; Chavarría et al. 2008). It possibly supports the youth of the region and a site of further ongoing star formation. It is also to be noted that the YSO surface density is associated with the PDR region, on the edge of bubbles. The correlation of cold dust,

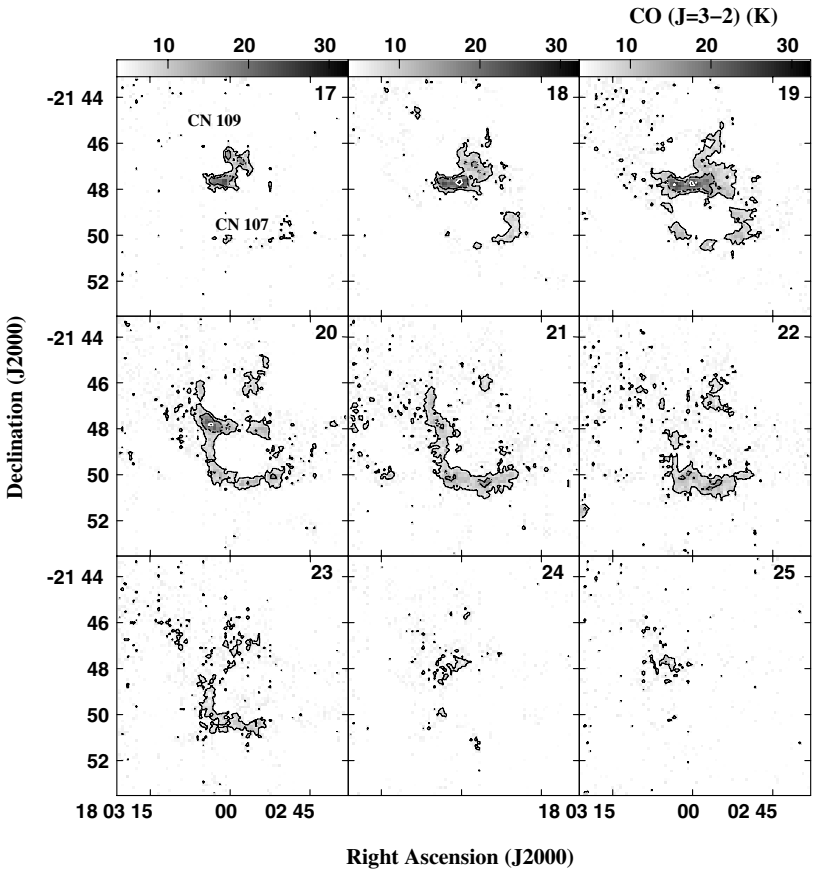

Figure 6. ^{12}CO(J = 3–2) channel maps in 1 km s^{-1} steps with velocity interval between 17 and 25 km s^{-1} around the G8.14+0.23 region. The gray color scale bar at the top is presented in unit of K in the range of 4–32 K and the contours are plotted for 6.4, 12.8, and 25.7 K, from outer to inner side. The bubbles CN 107 and CN 109 are also labeled in the top left panel.

Table 1
NIR and *Spitzer* IRAC/*GLIMPSE* Photometric Magnitudes are Listed for Selected Clustered YSOs Having Less Than or Equal to d_c Value Close to the Submillimeter Peak (See the Text)

Source	R.A. [2000]	Decl. [2000]	J (mag)	H (mag)	K_s (mag)	Ch1 (mag)	Ch2 (mag)	Ch3 (mag)	Ch4 (mag)	$\alpha_{\rm IRAC}$
IRS 1	18:03:00.94	−21:48:07.3	...	...	13.44 ± 0.01	8.79 ± 0.01	7.29 ± 0.01	6.07 ± 0.03	4.67 ± 0.04	1.85
IRS 2	18:03:00.59	−21:48:10.5	...	...	...	≪11.78	10.39 ± 0.10	7.68 ± 0.05	6.13 ± 0.07	3.96
IRS 3	18:03:00.36	−21:48:23.5	15.97 ± 0.01	13.76 ± 0.00	12.50 ± 0.00	11.44 ± 0.08	10.83 ± 0.09	...	...	...
IRS 4	18:03:01.12	−21:48:01.9	16.63 ± 0.02	14.98 ± 0.01	13.54 ± 0.01	11.10 ± 0.14	9.43 ± 0.10	...	...	...
IRS 5	18:03:02.90	−21:48:23.1	...	...	15.27 ± 0.03	11.54 ± 0.02	9.92 ± 0.02	8.71 ± 0.04	7.44 ± 0.06	1.81
IRS 6	18:03:03.70	−21:48:45.8	17.94 ± 0.05	15.87 ± 0.02	14.51 ± 0.01	13.14 ± 0.05	12.59 ± 0.07	...	...	...
IRS 7	18:03:04.33	−21:47:46.1	15.20 ± 0.01	14.39 ± 0.01	13.88 ± 0.01	13.44 ± 0.08	13.05 ± 0.10	...	...	...
IRS 8	18:03:04.39	−21:48:31.1	...	...	15.72 ± 0.04	11.27 ± 0.01	9.47 ± 0.01	8.55 ± 0.01	7.79 ± 0.02	1.03

Note. Spectral index ($\alpha_{\rm IRAC}$) was obtained by fitting of IRAC wavelengths (sources having at least three IRAC wavelengths magnitude).

molecular gas, ionized gas, and YSO surface density is shown in Figure 10(b). The association of YSOs with the collected materials around the region further reveals the ongoing star formation on the edge of bubbles.

In addition, we have checked the possibility of intrinsically "red sources" contamination, such as asymptotic giant branch (AGB) stars in our YSO sample. Recently, Robitaille et al. (2008) prepared an extensive catalog of such red sources based on the *Spitzer GLIMPSE* and MIPSGAL surveys. They showed that two classes of sources are well separated in the [8.0–24.0] color space such that YSOs are redder than AGB stars in this space (see also Whitney et al. 2008). Since, MIPS 24 μm data are saturated for the G8.14+0.23 region, we have therefore used criteria based on the IRAC magnitude (4.5 μm) and color space ([4.5–8.0]), to estimate the AGB contamination. It is believed that the presence of AGB stars in the cluster is unlikely (see Dewangan & Anandarao 2011, and references therein). Therefore, we have applied red source criteria for only those YSOs which are not cluster members with larger than d_c value (see Figure 10(a)). We find that *GLIMPSE* YSOs may be contaminated by AGB stars up to about 36% (5 out of 14 YSOs, see Section 3.3.1).

3.3.3. SED Modeling of Clustered YSOs

In this section, we present SED modeling of some selected YSOs to derive their various physical parameters using an online SED modeling tool (Robitaille et al. 2006, 2007). Clustering analysis of identified YSOs reveals that there is a grouping of

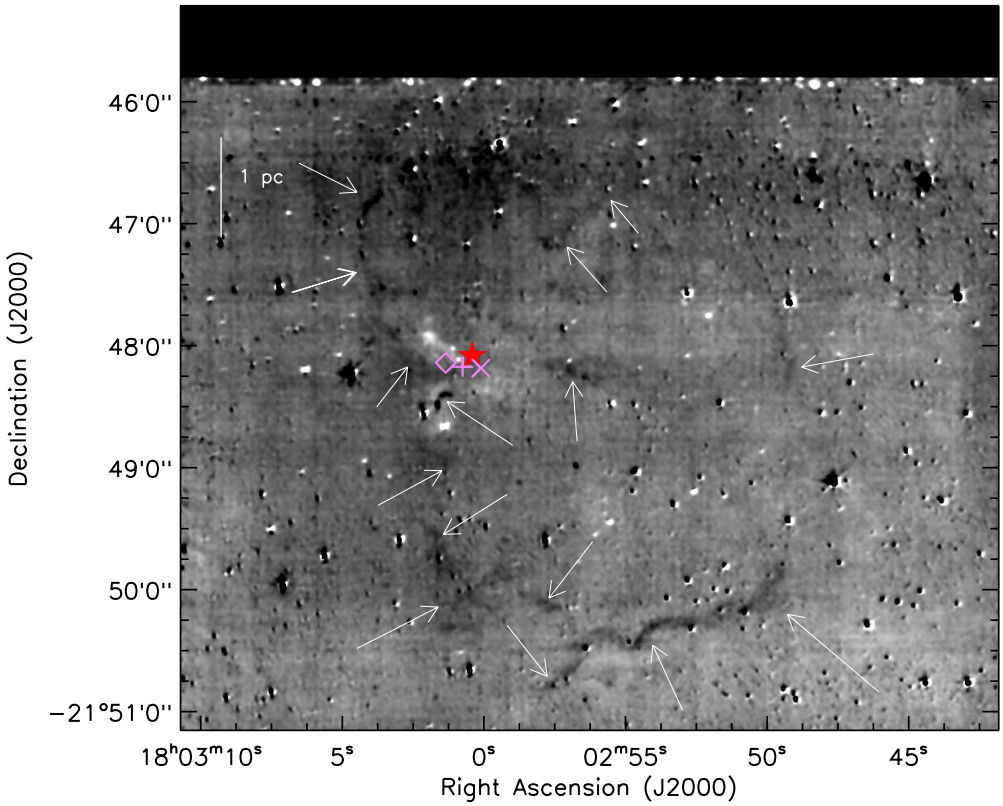

Figure 7. Inverted gray-scale image of the continuum-subtracted H_2 image at 2.12 μm. White arrows indicate the detected H_2 emission along the bubbles (as seen in *GLIMPSE* images) around the G8.14+0.23 region. The other marked symbols are similar to as shown in Figure 1. The continuum-subtracted H_2 image is processed to median filtering with a width of 4 pixels and smoothened by 4 × 4 pixels using boxcar algorithm to trace out the faint features in the image.

(A color version of this figure is available in the online journal.)

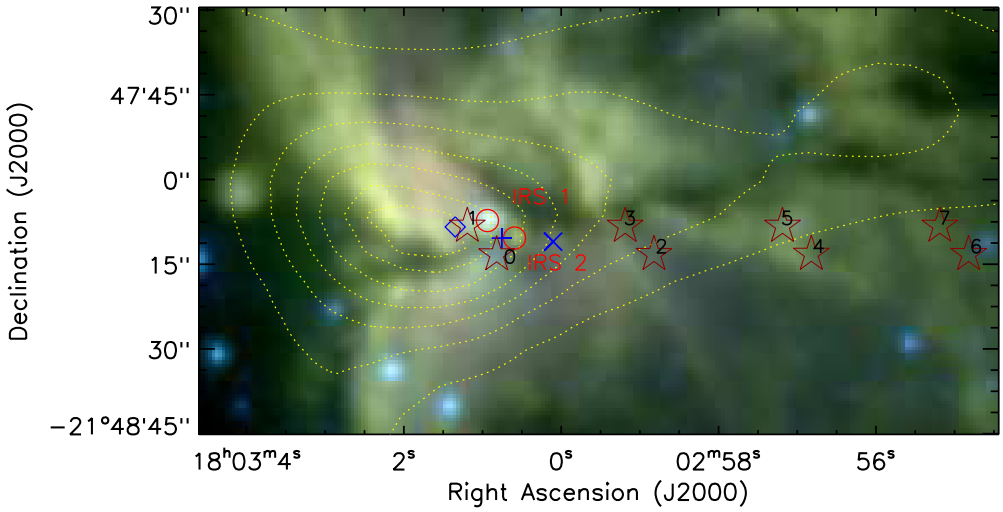

Figure 8. Zoomed-in three color composite image using IRAC 4.5 μm (blue), 5.8 μm (green), and 8.0 μm (red) around the G8.14+0.23 region (size ∼ 2.36 × 1.26 arcmin^2, as shown by a dashed box in Figure 1). Star symbols represent eight positions of *Spitzer*-IRS slit around the G8.14+0.23 region and also labeled as 0–7. SCUBA 850 μm emission is also shown by dotted yellow contours with similar levels as shown in Figure 2. The positions of IRS 1 and IRS 2 sources are marked by red circles and labeled in the image.

(A color version of this figure is available in the online journal.)

YSOs (∼20 YSOs pc^{-2}) close to the peak of the dense molecular gas and the dust clump in the region (see Figure 10(b)). We have selected eight YSOs (designated as IRS 1, ..., IRS 8) from this cluster close to the dense clump, which are detected at least up to *GLIMPSE* 4.5 μm or longer wavelengths for SED modeling. NIR and *Spitzer* IRAC/*GLIMPSE* photometric magnitudes for these selected YSOs are listed in Table 1 along with IRAC spectral indices (α_{IRAC}) and are also labeled in Figure 10(b). IRAC spectral indices were calculated using a least-squares fit to the IRAC flux points in a log(λ) versus log(λF_λ) diagram for those sources that are detected in at least three IRAC bands (see Dewangan & Anandarao 2011 for details). We have not included the MIPS 24 μm magnitude for SED modeling because the image is saturated close to the *IRAS* position. The SED model

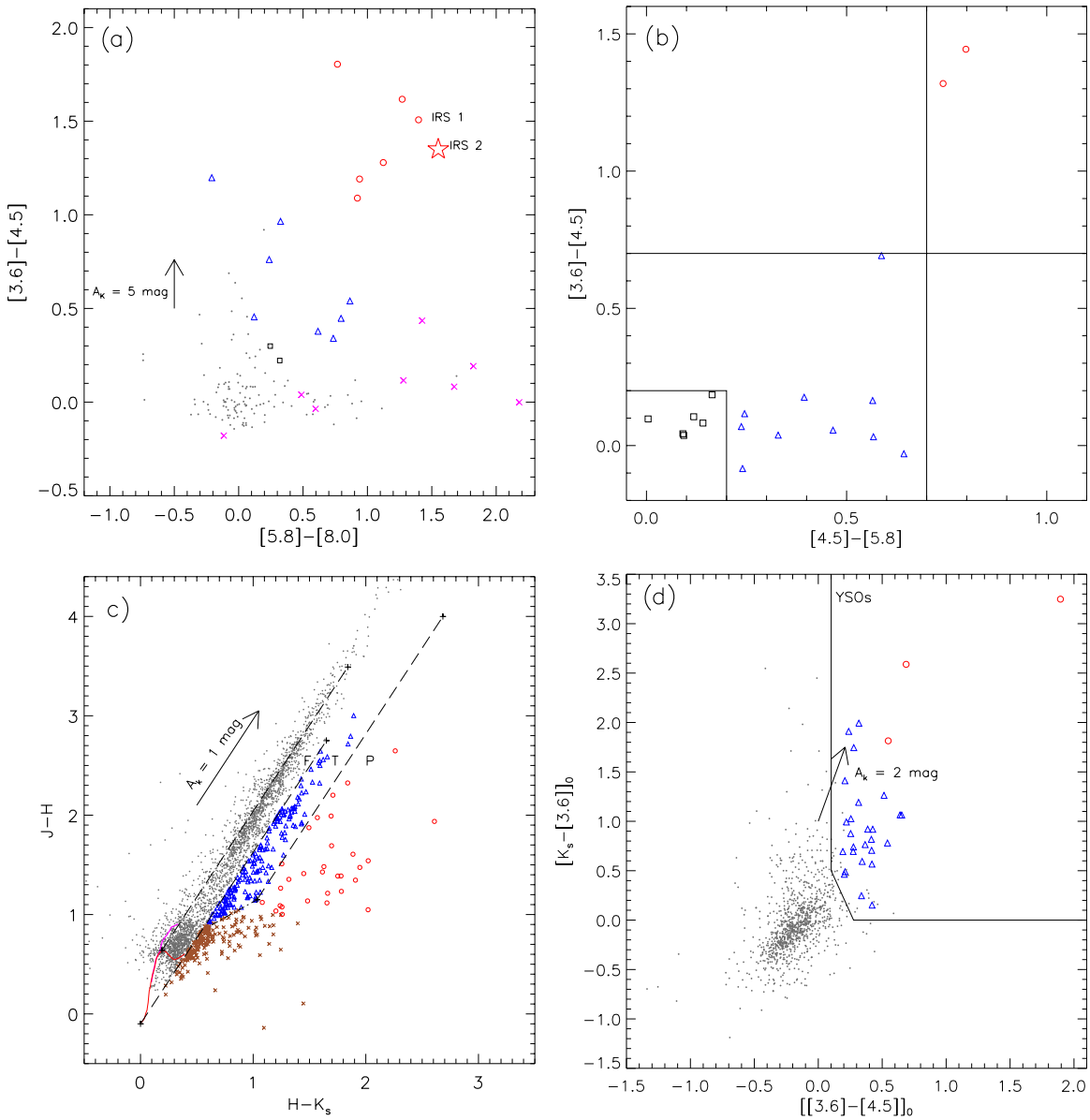

Figure 9. (a) Color–color diagram (CCD) using the *Spitzer*-IRAC four bands for all the sources identified within the region shown in Figure 1. The extinction vector for $A_K = 5$ mag is shown by an arrow, using the average extinction law from Flaherty et al. (2007). The dots in gray around the center (0,0) locate the stars with only photospheric emissions. The open squares (black), open triangles (blue), and open circles (red) represent Class III, Class II, and Class 0/I sources, respectively, classified using the $\alpha_{\rm IRAC}$ criteria. The "×" symbols in magenta show the identified PAH-emission-contaminated apertures in the region. The source IRS 2 is marked by a red star symbol and is also labeled along with the source IRS 1 in the diagram (see the text). (b) CC-D of the sources detected in three IRAC/*GLIMPSE* bands, except 8.0 μm. The open squares (black), open triangles (blue), and open circles (red) represent Class III, Class II, and Class 0/I sources, respectively, classified following the criteria suggested by Hartmann et al. (2005) and Getman et al. (2007). (c) UKIDSS JHK_s CC-D for the G8.14+0.23 region. UKIDSS NIR (JHK_s) magnitudes are calibrated in 2MASS system. The unreddened dwarf and giants loci are shown by red and magenta curves (Bessell & Brett 1988), respectively. The long-dashed straight lines across the CC-D are the extinction vectors ($A_K = 3$ mag) using Indebetouw et al. (2005) extinction law. The extinction vector $A_K = 1$ mag is also shown in the diagram. Classical T Tauri (CTTS) locus (in California Institute of Technology (CIT) system; Meyer et al. 1997) is shown by a dashed-dotted line. The loci of unreddened dwarf (Bessell & Brett (BB) system), giant (BB-system), and CTTS (CIT system) are converted into the 2MASS system using transformation equations given by Carpenter (2001). Red circles and open blue triangles represent the Class I and Class II YSOs. The CC-D is classified into three regions, namely, "F," "T," and "P" (see the text for details). (d) Figure shows the de-reddened $[K_s-[3.6]]_0$ vs. $[[3.6]-[4.5]]_0$ CC-D using NIR and *GLIMPSE* data. The selected region shown by the solid lines represents the location of YSOs. The extinction vector for $A_K = 2$ mag is shown by an arrow, calculated using the average extinction law from Flaherty et al. (2007). Open red circles and open blue triangles represent Class I and Class II sources, respectively.

(A color version of this figure is available in the online journal.)

tool requires a minimum of three data points with good quality as well as the distance to the source and visual extinction value. A distance range of 3.7–4.7 kpc and the visual extinction in the range from 8 to 25 mag are used as input parameters in SED modeling tool for each source to constraint the SEDs. These models assume an accretion scenario with a central source associated with rotationally flattened infalling envelope, bipolar cavities, and a flared accretion disk, all under radiative equilibrium. The model grid consists of 20,000 models of two-dimensional Monte Carlo simulations of radiation transfer with 10 inclination angles, resulting in a total of 200,000 SED models. The grid of SED models covers the mass range from 0.1 to 50 $M_\odot$. Only those models are selected that satisfy the criterion $\chi^2 - \chi^2_{\rm best} < 3$, where χ^2 is taken per data point. The plots of

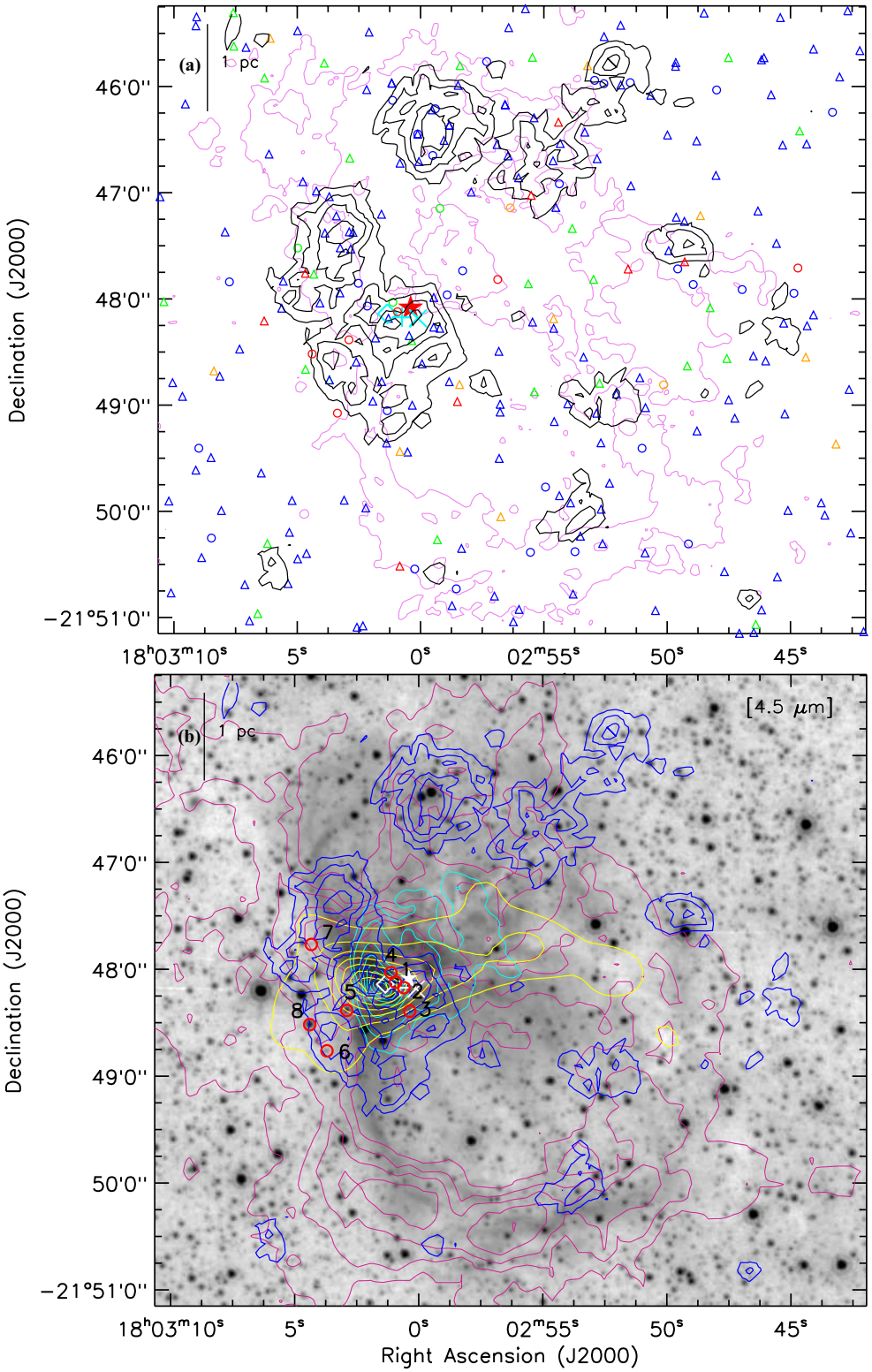

Figure 10. (a) The spatial distribution of all identified YSOs in the G8.14+0.23 region. The YSO surface density contours are plotted for 6, 8, 11, and 16 YSOs pc^{-2}, from outer to inner side (see the text for details). The open circles and open triangles show the Class I and Class II sources, respectively. The YSOs identified using four IRAC, three IRAC, NIR-IRAC, and NIR data are shown by red, orange, green, and blue, respectively. The Ch3/Ch2 ratio contours in violet are also overlaid on the image with a similar level as in Figure 4 and other marked symbols are similar to as shown in Figure 1. (b) The schematic represents the spatial distribution of YSOs, dust emission, molecular gas, and ionized gas in the G8.14+0.23 region. *GLIMPSE* 4.5 μm image is overlaid with contours of YSO surface density (blue; similar levels as in (a)), SCUBA 850 μm (yellow), MAGPIS 20 cm (cyan), and JCMT CO 3–2 (violet red) data. The CO 3–2 contour levels are 20%, 29%, 40%, 55%, 70%, and 80% of the peak, i.e., 139.551 K km s^{-1}. The contour levels of SCUBA 850 μm and MAGPIS 20 cm are similar to as shown in Figure 2. The selected clustered YSOs (see Section 3.3.3) are also marked (red circles) and labeled as 1, ..., 8 on the image (see Table 1).

(A color version of this figure is available in the online journal.)

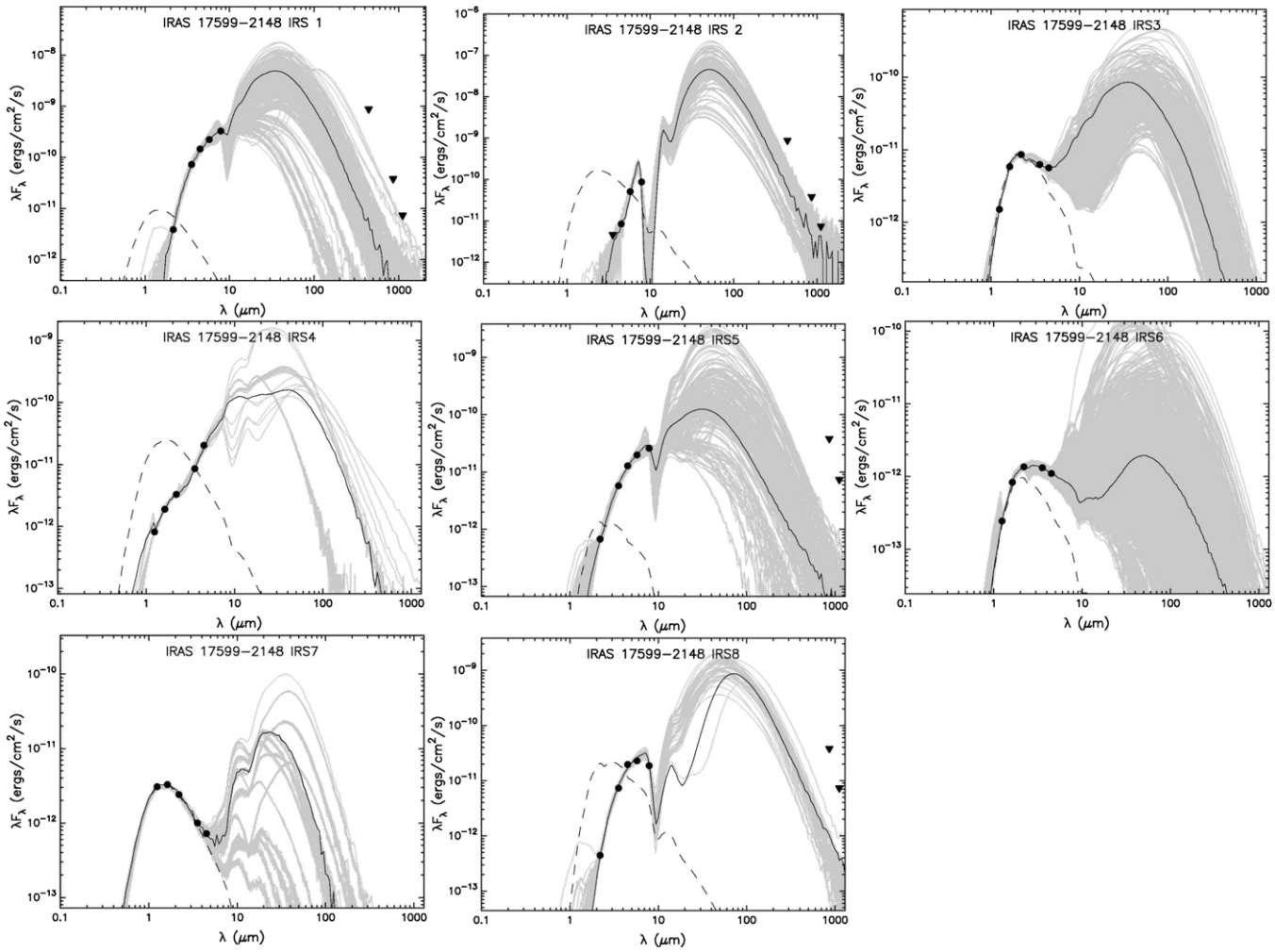

Figure 11. SED plots of all the selected sources. Filled circles are observed fluxes of good quality (with filled triangles as upper limits) taken from the archives or published literature (see the text for more details) and the curves show the fitted model with criteria $\chi^2 - \chi^2_{\rm best} < 3$. The thin black curve corresponds to the best-fitting model. The dashed curves represent photospheric contributions.

Table 2
Physical Parameters Derived from SED Modeling of the Selected Clustered YSOs (See the Text)

Source Name	Age log(yr)	M_* ($M_\odot$)	T_* log(T(K))	L_* log($L_\odot$)	$\dot{M}_{\rm env}$ log($M_\odot$ yr^{-1})	$\dot{M}_{\rm disk}$ log($M_\odot$ yr^{-1})	A_V (mag)	Degeneracy/ No. of Models
IRS 1	5.17 ± 0.72	10.33 ± 2.11	4.23 ± 0.26	3.74 ± 0.26	-4.19 ± 2.06	-6.96 ± 1.28	19.55 ± 5.47	316
IRS 2	3.86 ± 0.24	22.40 ± 2.61	4.01 ± 0.16	4.49 ± 0.20	-2.96 ± 0.12	-5.97 ± 0.51	17.63 ± 2.48	158
IRS 3	4.92 ± 0.37	3.51 ± 1.07	3.66 ± 0.03	1.88 ± 0.18	-4.46 ± 0.64	-7.70 ± 1.09	13.19 ± 2.08	821
IRS 4	5.46 ± 0.86	6.75 ± 2.53	4.11 ± 0.26	3.13 ± 0.56	-4.93 ± 1.84	-8.77 ± 2.71	13.63 ± 3.85	40
IRS 5	4.50 ± 1.09	5.01 ± 2.40	3.79 ± 0.27	2.53 ± 0.45	-4.58 ± 2.05	-6.36 ± 1.38	19.49 ± 5.13	376
IRS 6	5.73 ± 0.55	2.47 ± 0.97	3.69 ± 0.09	1.24 ± 0.29	-6.15 ± 1.62	-8.49 ± 1.68	14.12 ± 2.12	3271
IRS 7	6.43 ± 0.18	4.51 ± 0.75	4.16 ± 0.09	2.52 ± 0.24	-7.90 ± 0.17	-12.63 ± 0.83	8.13 ± 0.10	154
IRS 8	4.60 ± 0.59	7.80 ± 1.11	3.80 ± 0.17	3.04 ± 0.23	-3.61 ± 0.31	-6.63 ± 1.34	18.00 ± 5.82	48

SED fitted models are shown in Figure 11 for all the selected sources. The weighted mean values of the physical parameters (age, mass, temperature, luminosity, envelope accretion rate ($\dot{M}_{\rm env}$), and disk accretion rate ($\dot{M}_{\rm disk}$)) along with the standard deviations derived from the SED modeling for all the selected sources are given in Table 2. The table also contains the model-derived weighted mean values of A_V with standard deviations and the degeneracy of the models (i.e., the number of models that satisfy the χ^2 criterion as mentioned above). The derived SED model parameters show that the average value of mass, age, and A_V of these clustered YSOs are about 7.8 $M_\odot$, 0.12 Myr, and 15.5 mag, respectively. It is interesting to note that the embedded IRS 1 and IRS 2 sources are young and massive protostars. Finally, the SED modeling results favor the ongoing star formation around the region with detection of young YSOs as well as some massive candidates in their early phase of formation.

3.4. Star Formation Scenario

We have found evidence of collected material along the bubbles and also ongoing formation of YSOs on the edge of the bubbles. The morphology and distribution of YSOs suggest

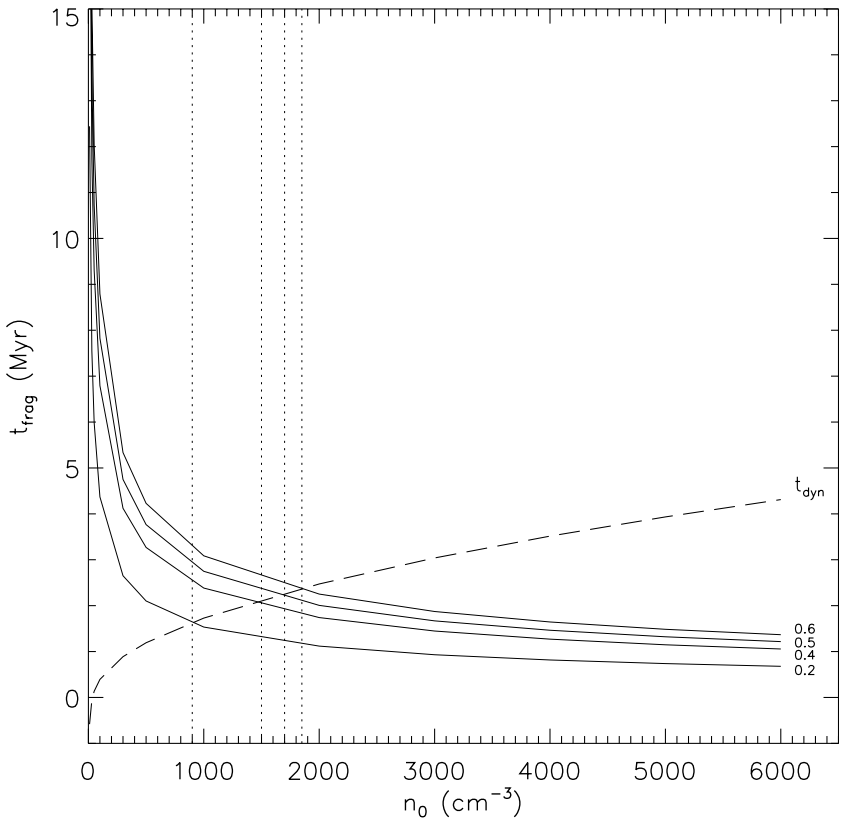

Figure 12. Schematic diagram shows the variation of fragmentation timescale (t_{frag}) and dynamical time (t_{dyn}) with initial density (n_0) of the ambient neutral medium. The fragmentation timescale is calculated for different turbulent velocity (a_s = 0.2, 0.4, 0.5, and 0.6 km s^{-1}). Dotted black lines indicate the value of "n_0" at which "t_{dyn}" is equal to "t_{frag}" for different "a_s" values.

that the G8.14+0.23 region is a site of star formation possibly triggered by the expansion of the H II region. In recent years, the triggered star formation process, especially "collect and collapse" mechanism has been studied extensively on the edges of many H II regions such as Sh 2-104, RCW 79, Sh 2-212, RCW 120, Sh 2-217 (Deharveng et al. 2003, 2008, 2009; Zavagno et al. 2006, 2010; Brand et al. 2011). In order to check the "collect and collapse" process as triggering mechanism around the G8.14+0.23 region, we have calculated the dynamical age (t_{dyn}) of the H II region and compared it with an analytical model by Whitworth et al. (1994). We have estimated the age of the H II region at a given radius R, using the following equation (Dyson & Williams 1980):

$$t_{dyn} = \left(\frac{4\,R_s}{7\,c_s}\right)\left[\left(\frac{R}{R_s}\right)^{7/4} - 1\right], \quad (1)$$

where c_s is the isothermal sound velocity in the ionized gas (c_s = 10 km s^{-1}) and R_s is the radius of the Strömgren sphere, given by $R_s = (3N_{uv}/4\pi n_0^2 \alpha_B)^{1/3}$, where the radiative recombination coefficient $\alpha_B = 2.6\times10^{-13}\,(10^4\,K/T)^{0.7}$ cm^3 s^{-1} (Kwan 1997). In this calculation, we have used $\alpha_B = 3.9 \times 10^{-13}$ cm^3 s^{-1} for the temperature of 5600 K (see Kim & Koo 2001). N_{uv} is the total number of ionizing photons per unit time, emitted by ionizing stars and "n_0" is the initial particle number density of the ambient neutral gas. We have adopted the Lyman continuum photon flux value (N_{uv} =) of 1.2 × 10^{49} ph s^{-1} (log N_{uv} = 49.1) from Kim & Koo (2001) for an electron temperature, distance, and integrated 21 cm (1.43 GHz) flux density of 5600 K, 4.2 kpc, and 6.67 Jy, respectively. We have estimated the ambient density (n_0 =) 3575.7 cm^{-3} of the H II region using ^{12}CO(J = 3–2) line data (see Section 3.2). Using N_{uv}, a mean radius of the H II region (R =) 5.9 pc (see Kim & Koo 2001), and n_0 = 3575.7 cm^{-3}, we have obtained t_{dyn} ∼ 3.3 Myr using Equation (1). Following, Whitworth et al. (1994) analytical model for the "collect and collapse" process, we have estimated a fragmentation timescale (t_{frag}) of 0.86–1.73 Myr for a turbulent velocity (a_s =) of 0.2–0.6 km s^{-1} in the collected layer. We have found that dynamical age is larger than fragmentation timescale for n_0 = 3575.7 cm^{-3}. We have plotted the variation of t_{frag} and t_{dyn} with initial density (n_0) of the ambient neutral medium (see Figure 12). The t_{frag} is also calculated for different turbulent velocities in Whitworth et al. (1994) model. It is to be noted that if t_{dyn} is larger than t_{frag}, then ambient density (n_0) should be larger than 900, 1500, 1700, and 1850 cm^{-3} for different "a_s" values of 0.2, 0.4, 0.5, and 0.6 km s^{-1}, respectively (see Figure 12). We have also estimated the kinematical timescale of molecular bubbles of about 1 Myr (∼4 pc/4 km s^{-1}), assuming bubble size of about 4 pc and velocity dispersion ∼4 km s^{-1} from ^{12}CO(J = 3–2) map (see Section 3.2). The comparison of the dynamical age of the H II region and the kinematical timescale of expanding bubbles with the fragmentation timescale further supports triggered star formation and indicates the fragmentation of the molecular materials into clumps due to "collect and collapse" process around the bubbles. Further, the spatial distribution and the clustering analysis of YSOs show the association of YSO clusters in the north, east, west, and southeast regions with molecular material along the bubbles. Among these, the average age of selected eight YSOs, including IRS 1 and IRS 2 (see Section 3.3.3), is about 0.12 Myr (estimated from SED modeling), which is less than the dynamical age of the H II

region. We have also found that these two sources (IRS 1 and IRS 2) are young and massive embedded protostars (about 10 and 22 $M_{\odot}$) associated with the dense clump at the interface of the bubbles. It seems that the YSOs present on the edges of the bubbles are associated with the collected and fragmented molecular clumps, possibly by the "collect and collapse" process (see Kang et al. 2009; Pomarés et al. 2009; Paron et al. 2011). This scenario is further supported by the detection of massive YSOs (IRS 1 and IRS 2) associated with the dense clump. However, one cannot entirely rule out the possibility of triggered star formation by compression of the pre-existing dense clumps by the shock wave. It is therefore difficult to distinguish the star formation scenario from the pre-existing condensations and/or by the "collect and collapse" process in our selected region with the available data presented in this work.

Recently, Onaka et al. (2009) reported very broad emission features around 22 μm in some MSF regions (viz., Cas A, Carina nebula, and Sharpless 171) and suggested that this feature possibly originated from the dust grains formed in the supernova. Since the G8.14+0.23 region is about 0.3 deg away from the W30 supernova remnant (SNR) and *Spitzer*-IRS spectroscopic observations are available for this region in the wavelength range of 20–36.5 μm, it is possible to explore the signature of the supernova-induced star formation activity around this region. Following Onaka et al. (2009), we therefore re-examined the *Spitzer*-IRS processed archival spectra (AOR:14928896; PI: Yoko Okada) obtained from "*Spitzer* Heritage Archive[6]" around the G8.14+0.23 region (see IRS slit positions in Figure 8 and also Okada et al. 2008). We, however, did not find any broad feature around 22 μm (see also Table 2 of Okada et al. 2008). Hence, we may reject the possibility of the supernova-induced star formation activity in the G8.14+0.23 region. Ojeda-May et al. (2002) studied nine MSF regions, including G8.14+0.23, in the vicinity of the W30 SNR using 6 cm radio observation and they also ruled out the possibility of a supernova-induced star formation based on the 6 cm detection around this region and age consideration of the W30 SNR.

4. CONCLUSIONS

We have explored the triggered star formation scenario around two bubbles associated with a southern MSF region G8.14+0.23 using multi-wavelength observations. We find that there is a clear evidence of collected material (molecular and cold dust) along the bubbles around the G8.14+0.23 region. The JCMT CO velocity map reveals that the molecular gas in the bubbles is physically associated around the region G8.14+0.23. The surface density of YSOs reveals ongoing star formation and clustering of YSOs associated with the edge of the bubbles. We conclude that the YSOs are being formed on the edge of the bubbles possibly by the expansion of the H II region. We further investigated the "collect and collapse" process for triggered star formation around the G8.14+0.23 region using analytical model of Whitworth et al. (1994). We have found that the dynamical age (~3.3 Myr) of the H II region is larger, and the kinematical timescale of bubbles (~1 Myr) is comparable to the fragmentation timescale (~0.86–1.73 Myr) of accumulated gas layers in the region for 3575.7 cm^{-3} ambient density. The comparison of the dynamical age and the kinematical timescale of expanding bubbles with the fragmentation timescale further supports triggered star formation and indicates the fragmentation of the molecular materials into clumps possibly due to the "collect and collapse" process around the G8.14+0.23 region. We have also investigated infrared counterparts of two young massive embedded protostars (about 10 and 22 $M_{\odot}$) associated with dense clumps at the interface of the bubbles. It seems that the expansion of the H II region is also leading to the formation of these two young massive embedded YSOs in the G8.14+0.23 region. Our study possibly favors the "collect and collapse" scenario for the formation of YSOs around the bubbles in the G8.14+0.23 region. However, we cannot entirely rule out the possibility of triggered star formation by compression of the pre-existing dense clumps by the shock wave.

We thank the anonymous referee for a critical reading of the paper and several useful comments and suggestions, which greatly improved the scientific content of the paper. This work is based on data obtained as part of the UKIRT Infrared Deep Sky Survey and UWISH2 survey. This publication made use of data products from the Two Micron All Sky Survey (a joint project of the University of Massachusetts and the Infrared Processing and Analysis Center/California Institute of Technology, funded by NASA and NSF), archival data obtained with the *Spitzer Space Telescope* (operated by the Jet Propulsion Laboratory, California Institute of Technology under a contract with NASA). We thank Dirk Froebrich for providing the narrowband H_2 image through the UWISH2 survey.

[6] See http://irsa.ipac.caltech.edu/applications/Spitzer/SHA/.

REFERENCES

Aguirre, J. E., Ginsburg, A. G., Dunham, M. K., et al. 2011, ApJS, 192, 4
Benjamin, R. A., Churchwell, E., Babler, B. L., et al. 2003, PASP, 115, 953
Bessell, M. S., & Brett, J. M. 1988, PASP, 100, 1134
Brand, J., Massi, F., Zavagno, A., Deharveng, L., & Lefloch, B. 2011, A&A, 527, 62
Carey, S. J., Noriega-Crespo, A., Price, S. D., et al. 2005, BAAS, 37, 1252
Carpenter, J. M. 2001, AJ, 121, 2851
Casali, M., Adamson, A., Alves de Oliveira, C., et al. 2007, A&A, 467, 777
Cesaroni, R., Walmsley, C. M., & Churchwell, E. 1992, A&A, 256, 618
Chavarría, L. A., Allen, L. E., Hora, J. L., et al. 2008, ApJ, 682, 445
Churchwell, E., Babler, B. L., Meade, M. R., et al. 2009, PASP, 121, 213
Churchwell, E., Povich, M. S., Allen, D., et al. 2006, ApJ, 649, 759
Churchwell, E., Walmsley, C. M., & Cesaroni, R. 1990, A&AS, 83, 119
Churchwell, E., Watson, D. F., Povich, M. S., et al. 2007, ApJ, 670, 428
Codella, C., Felli, M., Natale, V., Palagi, F., & Palla, F. 1994, A&A, 291, 261
Deharveng, L., Lefloch, B., Kurtz, S., et al. 2008, A&A, 482, 585
Deharveng, L., Lefloch, B., Zavagno, A., et al. 2003, A&A, 408, L25
Deharveng, L., Zavagno, A., Schuller, F., et al. 2009, A&A, 496, 177
Dewangan, L. K., & Anandarao, B. G. 2011, MNRAS, 414, 1526
Di Francesco, J., Johnstone, D., Kirk, H., MacKenzie, T., & Ledwosinska, E. 2008, ApJS, 175, 277
Dye, S., Warren, S. J., Hambly, N. C., et al. 2006, MNRAS, 372, 1227
Dyson, J. E., & Williams, D. A. 1980, Physics of the Interstellar Medium (New York: Halsted Press), 204
Fazio, G. G., Hora, J. L., Allen, L. E., et al. 2004, ApJS, 154, 10
Flaherty, K. M., Pipher, J. L., Megeath, S. T., et al. 2007, ApJ, 663, 1069
Froebrich, D., Davis, C. J., Ioannidis, G., et al. 2011, MNRAS, 413, 480
Getman, K. V., Feigelson, E. D., Garmire, G., Broos, P., & Wang, J. 2007, ApJ, 654, 316
Gutermuth, R. A., Megeath, S. T., Myers, P. C., et al. 2009, ApJS, 184, 18
Gutermuth, R. A., Pipher, J. L., Megeath, S. T., et al. 2011, ApJ, 739, 84
Hartmann, L., Megeath, S. T., Allen, L., et al. 2005, ApJ, 629, 881
Helfand, D. J., Becker, R. H., White, R. L., Fallon, A., & Tuttle, S. 2006, AJ, 131, 2525
Hodgkin, S. T., Irwin, M. J., Hewett, P. C., & Warren, S. J. 2009, MNRAS, 394, 675
Indebetouw, R., Mathis, J. S., Babler, B. L., et al. 2005, ApJ, 619, 931
Ji, W.-G., Zhou, J.-J., Esimbek, J., et al. 2012, A&A, 544, A39
Kang, M., Bieging, J. H., Kulesa, C. A., & Lee, Y. 2009, ApJ, 701, 454
Kim, K. T., & Koo, B. C. 2001, ApJ, 549, 979
Kim, K. T., & Koo, B. C. 2003, ApJ, 596, 362
Kumar, D. L., & Anandarao, B. G. 2010, MNRAS, 407, 1170
Kwan, J. 1997, ApJ, 489, 284

Lawrence, A., Warren, S. J., Almaini, O., et al. 2007, MNRAS, 379, 1599
Meyer, M. R., Calvet, N., & Hillenbrand, L. A. 1997, AJ, 114, 288
Ojeda-May, P., Kurtz, S. E., Rodrígurez, L. F., Arthur, S. J., & Velázquez, P. 2002, RevMexAA, 38, 111
Ojha, D. K., Kumar, M. S. N., Davis, C. J., & Grave, J. M. C. 2010, MNRAS, 407, 1807
Ojha, D. K., Tamura, M., Nakajima, Y., et al. 2004a, ApJ, 608, 797
Ojha, D. K., Tamura, M., Nakajima, Y., et al. 2004b, ApJ, 616, 1042
Okada, Y., Onaka, T., Miyata, T., et al. 2008, ApJ, 682, 416
Onaka, T., Roellig, T. L., Okada, Y., & Chan, K. W. 2009, in The Fourth Spitzer Science Center Conf., The Evolving ISM in the Milky Way and Nearby Galaxies, Pasadena, CA, 2007 December 2–5, ed. K. Sheth, A. Noriega-Crespo, J. Ingalls, & R. Paladini, 11, http://ssc.spitzer.caltech.edu/mtgs/ismevol/
Paron, S., Petriella, A., & Ortega, M. E. 2011, A&A, 525, 132
Pomarés, M., Zavagno, A., Deharveng, L., et al. 2009, A&A, 494, 987
Povich, M. S., Stone, J. M., Churchwell, E., et al. 2007, ApJ, 660, 346
Reach, W. T., Megeath, S. T., Cohen, M., et al. 2005, PASP, 117, 978
Reach, W. T., Rho, J., Tappe, A., et al. 2006, AJ, 131, 1479
Rieke, G. H., Young, E. T., Engelbracht, C. W., et al. 2004, ApJS, 154, 25
Robitaille, T. P., Meade, M. R., Babler, B. L., et al. 2008, AJ, 136, 2413
Robitaille, T. P., Whitney, B. A., Indebetouw, R., & Wood, K. 2007, ApJS, 169, 328
Robitaille, T. P., Whitney, B. A., Indebetouw, R., Wood, K., & Denzmore, P. 2006, ApJS, 167, 256
Rowles, J., & Froebrich, D. 2009, MNRAS, 395, 1640
Silk, J. 1997, ApJ, 481, 703
Skrutskie, M. F., Cutri, R. M., Stiening, R., et al. 2006, AJ, 131, 1163
Smith, M. D., & Rosen, A. 2005, MNRAS, 357, 1370
Stark, A. A., & Brand, J. 1989, ApJ, 339, 763
Stetson, P. B. 1987, PASP, 99, 191
Sugitani, K., Tamura, M., Nakajima, Y., et al. 2002, ApJ, 565, L25
Thompson, M. A., Hatchell, J., Walsh, A. J., MacDonald, G. H., & Millar, T. J. 2006, A&A, 453, 1003
Thompson, M. A., Urquhart, J. S., Moore, T. J. T., & Morgan, L. K. 2012, MNRAS, 421, 408
Varricatt, W. P. 2011, A&A, 527, 97
Walsh, A. J., Burton, M. G., Hyland, A. R., & Robinson, G. 1998, MNRAS, 301, 640
Walsh, A. J., Hyland, A. R., Robinson, G., & Burton, M. G. 1997, MNRAS, 291, 261
Watson, C., Corn, T., Churchwell, E. B., et al. 2009, ApJ, 694, 546
Watson, C., Hanspal, U., & Mengistu, A. 2010, ApJ, 716, 1478
Watson, C., Povich, M. S., Churchwell, E. B., et al. 2008, ApJ, 681, 1341
Whitney, B. A., Sewilo, M., Indebetouw, R., et al. 2008, AJ, 136, 18
Whitworth, A. P., Bhattal, A. S., Chapman, S. J., Disney, M. J., & Turner, J. A. 1994, MNRAS, 268, 291
Zavagno, A., Deharveng, L., Comeron, F., et al. 2006, A&A, 446, 171
Zavagno, A., Russeil, D., Motte, F., et al. 2010, A&A, 518, L81
Zinnecker, H., & Yorke, H. W. 2007, ARA&A, 45, 481